Journal of Materials Chemistry A

PAPER

View Article Online
View Journal | View Issue

Cite this: J. Mater. Chem. A, 2019, 7, 18380

Amorphous multinary phyllosilicate catalysts for electrochemical water oxidation†

Byunghoon Kim,‡[a] Ju Seong Kim,‡[c] Hyunah Kim,[ab] Inchul Park,[d] Won Mo Seong[a] and Kisuk Kang *[ab]

The practical realization of a water-splitting system necessitates the development of high-performance oxygen evolution reaction (OER) catalysts. Despite tremendous research efforts aimed at identifying earth-abundant 3d transition-metal-based catalysts, their insufficient catalytic efficiencies continue to jeopardize their real-world application. Herein, we introduce amorphous cobalt–iron phyllosilicates (ACFPs) as highly efficient OER catalysts. The ACFPs were designed by tailoring the metal chemistry of the phyllosilicate framework which consists of laminations of silicate (SiO_4) layers and layered Co–Fe (oxy)hydroxide motifs, and prepared using a facile room-temperature precipitation method. It is demonstrated that the OER properties/mechanisms are sensitively affected by the Co/Fe ratio, with an exceptionally low overpotential ($\eta \sim 329$ mV for a current density of 10 mA cm^{-2}) delivered at the optimized composition of 40 at% Fe. This catalytic efficiency is greater than that of the structurally analogous Co–Fe (oxy)hydroxide as well as those of pure Co or Fe phyllosilicate, suggesting the beneficial role of the phyllosilicate framework along with the synergistic interplay of Co and Fe ions in the framework. Density functional theory calculations revealed that the introduction of Fe at the surface of Co phyllosilicate perturbs the local structural environment of oxygen sites, providing additional active sites. This work proposes a valid strategy for the design of high-performance catalysts by chemically tuning both the redox-active and redox-inert elements concomitantly in novel multinary phyllosilicate-based OER catalysts.

Received 27th May 2019
Accepted 17th July 2019

DOI: 10.1039/c9ta05599a

rsc.li/materials-a

1. Introduction

Solar-power-driven water splitting is considered one of the most environmentally friendly and effective ways to produce hydrogen, a clean energy source that will enable a reduction of our reliance on fossil fuels.[1–5] The overall efficiency of the water-splitting reaction is primarily limited by the sluggish kinetics of the oxygen evolution reaction (OER), an anodic half reaction, which result from its complex multielectron pathways.[6–9] While some of the precious-metal-based OER catalysts have proven to be effective in catalyzing the water splitting reactions, first-row (3d) transition-metal–oxide-based materials have attracted a recent particular interest as more practically viable catalysts because of their low cost and sustainability.[10–14] Various structural motifs have been investigated in exploring the 3d transition-metal chemistry for OER catalysis, including layered (oxy)hydroxide, spinel, perovskite, and rock-salt-type metal oxide structures.[15–17] Catalysts with an amorphous phase represented by cobalt phosphate and nickel borate have also received tremendous attention because of their remarkable catalytic activity in neutral or weak alkaline electrolytes.[7,18] Structure and mechanistic analyses have revealed that the catalytically active units of these amorphous Co- and Ni-based catalysts are layered (oxy)hydroxides consisting of edge-sharing MO_6 octahedra layers.[19–22]

With the aim of developing a new platform for 3d transition-metal chemistry in OER catalysis, we recently reported an amorphous cobalt phyllosilicate (ACP) as an efficient and low-cost OER catalyst.[23] ACP was designed by introducing redox-inert silicate groups in the layer space of crystalline metal (oxy)hydroxide motifs. The presence of silicate groups in the layered motifs was demonstrated to significantly modulate the local environment of active sites, thus regulating the catalytic activity of the metal (oxy)hydroxide motifs in the structure. These structural modifications markedly enhanced the catalytic performance (an overpotential of ~367 mV for a current density

[a]Department of Materials Science and Engineering, Research Institute of Advanced Materials (RIAM), Seoul National University, 1 Gwanak-ro, Gwanak-gu, Seoul 151-742, Republic of Korea. E-mail: matlgen1@snu.ac.kr

[b]Center for Nanoparticle Research, Institute for Basic Science (IBS), Seoul National University, 1 Gwanak-ro, Gwanak-gu, Seoul 151-742, Republic of Korea

[c]Platform Material Team 2, R&D Center, Samsung SDI, 130, Samsungro, Yeongtong-gu, Suwon-si, Gyeonggi-do 16678, Republic of Korea

[d]RIST, POSCO Global R&D Center, 100, Songdogwahak-ro, Yeonsu-gu, Incheon, 21985, Republic of Korea

† Electronic supplementary information (ESI) available. See DOI: 10.1039/c9ta05599a

‡ Byung Kim and Ju Seong Kim equally conttributed to the work (co first authors).

of 10 mA cm^{-2}) compared with that of cobalt (oxy)hydroxide (which has a structure consisting of layered motifs of ACP without silicate groups), validating the promise of phyllosilicate motifs as a new framework for OER catalysts.

For a given catalyst structural framework, one of the facile routes to exploit the full chemistry is to introduce a diversity in the cations, since the interaction between different metals in the catalyst affects the electronic structure[24,25] and induces strain in the pristine geometry,[26,27] possibly leading to optimization of the energetics of the intermediates involved in the OER.[28–30] Substantial research has been conducted to uncover catalytically optimal combinations of metals for a given structure.[17,31,32] Benefiting from such synergistic interplay, some multi-metal–oxide-based catalysts have exhibited excellent catalytic properties, outperforming their single-metal counterparts.[11,24,33–36] In particular, Fe-containing Co- and Ni-based oxides are known to deliver one of the highest efficiencies toward the OER in alkaline conditions among 3d transition-metal-based catalysts.[34,35,37–41] The incorporation of Fe could improve the intrinsic activity of Co and Ni (oxy)hydroxides by approximately 100- and 500-fold, respectively.[34,35] Considering the structural similarities of layered (oxy)hydroxide and phyllosilicate groups, analogous multi-metal interactions are expected for both motifs, although the multinary metal system for the latter has not yet been documented.

Herein, we extend the chemistry of phyllosilicate catalysts to the binary Co–Fe system and report the exceptional OER properties of amorphous cobalt iron phyllosilicate (ACFP) catalysts. ACFPs with the full range of Co/Fe compositions are successfully synthesized from a facile and cost-effective co-precipitation method at room temperature. And, it is demonstrated that the synergistic role of Co and Fe in the ACFP phyllosilicate at a certain Co/Fe ratio leads to the OER activity that far outperforms other Co–Fe-based OER catalysts as well as those of pure cobalt and pure iron phyllosilicates. Theoretical investigations of ACFPs based on density functional theory (DFT) calculations reveal that the introduction of Fe into ACP causes the local structural modulation and provides an additional primary active site without compromising the activity of the existing active site, thereby improving the overall catalytic efficiencies. These findings suggest that the basic catalytic activity of layered (oxy)hydroxide motifs can be enriched not only by the structural modification, employing the redox-inert silicate groups in phyllosilicates, but also by the rational tuning of synergistic interplay between different cations in the structure, implying this dual approach can be an interesting new approach for the discovery of new high-performance catalysts.

2. Results and discussion

Phyllosilicate minerals are a class of earth-abundant layered silicate materials in which parallel silicate layers and metal layers are alternatively stacked, as schematically illustrated in Fig. 1a.[42] Each silicate layer consists of corner-shared $(SiO_4)^{2-}$ tetrahedra. Three of the four oxygens from each $(SiO_4)^{2-}$ tetrahedron are shared with other tetrahedra, forming interconnected hexagonal rings and leading to a basic structural unit of $(Si_2O_5)^{2-}$ (see Fig. 1b). On the other hand, the metal layer consists of edge-shared MO_6 (M: Mg, Al, Ca, Fe, Co, Ni, *etc.*) octahedra, and each MO_6 octahedron shares its apical oxygens with a $(SiO_4)^{2-}$ tetrahedron, such that one or two silicate sheets reside between metal layers. Considering the six-membered ring structure of the silicate layers, certain apical oxygens of the MO_6 octahedra do not bind to silicate layers at the center of the silicate rings, as indicated with a red circle in Fig. 1b. These apical oxygens have been demonstrated to be mostly hydrated, providing hydroxyl (OH^-) groups for the basal plane of metal layers.[43] We note that the MO_6 layers of phyllosilicate itself, except for the silicate layers, are isostructural to archetypal metal (oxy)hydroxides (MOOH) in that both take a brucite structure. In the present study, we prepared a series of cobalt–iron binary phyllosilicates, where M sites are occupied by Co and Fe.

The series of cobalt–iron phyllosilicates were synthesized *via* a simple co-precipitation reaction in which a metal chloride ($CoCl_2$ and $FeCl_2 \cdot 4H_2O$) aqueous solution was mixed with a Na_2SiO_3 aqueous solution at room temperature. The Co : Fe ratio in the precursors was altered by 20 at% from 100 : 0, 80 : 20, 60 : 40, 40 : 60, 20 : 80, and 0 : 100, which resulted in ACP, ACFP82, ACFP64, ACFP46, ACFP28 and AFP, respectively. Quantitative analysis using energy-dispersive X-ray spectroscopy (EDS) confirmed that the Co/Fe ratios in the final precipitates were consistent with the target compositions, indicating that no preferential precipitation occurs for a specific metal element and that accurate control of the composition is possible (see Table S1, ESI†). Fig. 2a presents X-ray diffraction (XRD) patterns of the as-prepared samples. Regardless of the metal composition, the diffraction patterns mainly consisted of broad peaks of characteristic phyllosilicate structures, signifying the amorphous nature of the precipitates. To obtain more detailed information about the crystalline motifs in the precipitates, the amorphous phyllosilicates were hydrothermally annealed at 180 °C for 24 hours. The XRD patterns of the annealed precipitates (Fig. 2b) were similar to those of the as-prepared precipitates except for the better-defined peaks. The XRD peaks of the annealed samples (~20° and 60°) matched well with the references of crystalline cobalt phyllosilicate ($Co_3Si_4O_{10}(OH)_2$, #21-0871) and iron phyllosilicate ($Fe_2Si_4O_{10}(OH)_2$, #42-0569). It is noted that the peak at 28° gets more pronounced with increasing Fe content in ACFPs, indicating that, with the addition of Fe, the precipitate phases were gradually converted to the iron phyllosilicate analogue phase.

The Fourier-transform infrared (FT-IR) spectra of the precipitates further verified that their local bonding characteristics correspond to those of typical phyllosilicates regardless of Co : Fe ratio. Fig. 2c and d present the FT-IR spectra of the as-prepared and annealed precipitates, respectively, with almost identical patterns displayed for the full range examined. The shoulder peaks at 3600 cm^{-1} correspond to the O–H stretching vibration mode (ν_{OH}) of the OH–3M (M: Co or Fe), which signifies the existence of apical hydroxyl (OH^-) groups of MO_6 layers located at the center of silicate rings. The low-wavenumber region consists of peaks associated with the

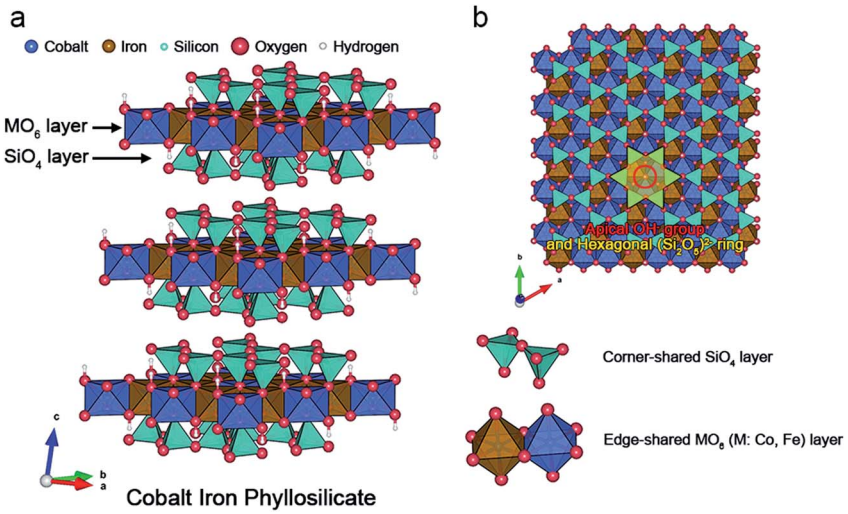

Fig. 1 Schematic representation of the crystal structure of ACFP, which consists of alternative stacking of corner-shared SiO_4 layers and edge-shared MO_6 (M: Co, Fe) layers: (a) front view and (b) top view.

corner-shared SiO_4 tetrahedra layer, where the peaks at 1000 cm^{-1} and 450 cm^{-1} are assigned to the Si–O bending vibration (δ_{SiO}) and asymmetric Si–O bending vibration (δ_{SiO}) modes, respectively.[44] The peak at 660 cm^{-1} corresponds to the superimposition of the Si–O stretching vibration (ν_{OH}) and O–H bending vibration modes (δ_{OH}) of the OH–3M (M: Co or Fe). Overall, the FT-IR spectra of the as-prepared and annealed precipitates for the full metal composition range consistently feature the bonding characteristics of the phyllosilicate phase. Combined with the results from the XRD analysis, the obtained precipitates can be characterized as an amorphous phase of cobalt–iron phyllosilicate (see ESI† for more details of the material characterizations and analyses). To probe the electronic states of the metal elements in the ACFPs, X-ray

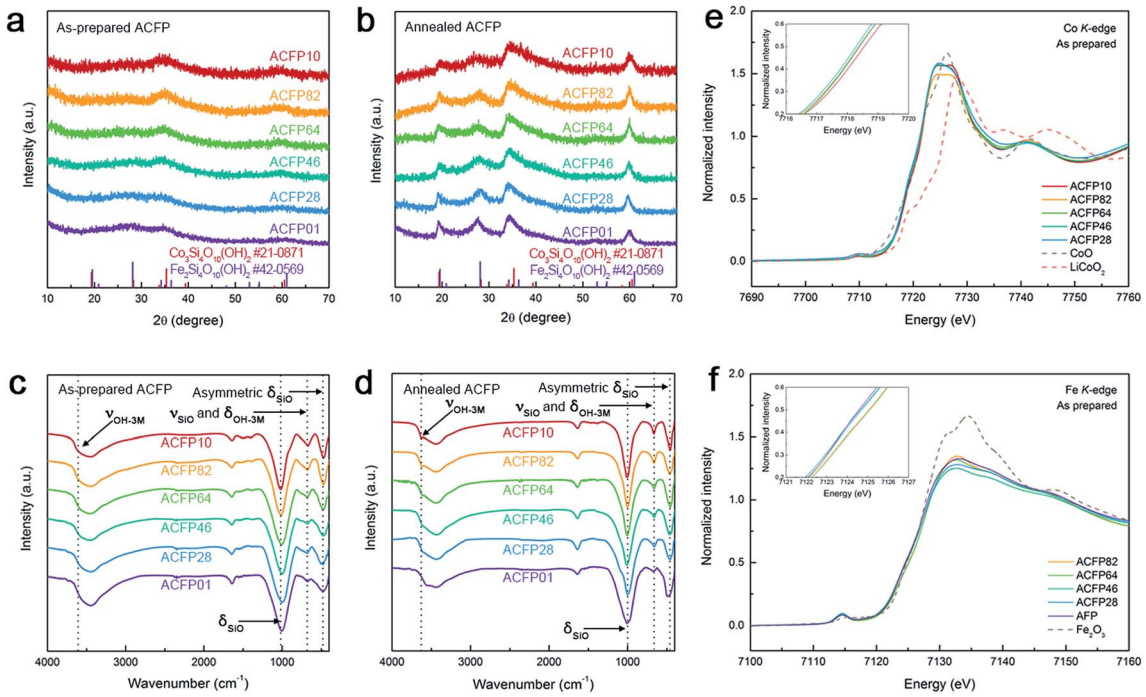

Fig. 2 Powder XRD patterns of (a) as-prepared and (b) hydrothermally annealed ACFP series. (c) and (d) indicate FT-IR spectra of as-prepared and hydrothermally annealed ACFP series, respectively. In (c) and (d), the broad band near 3500 cm^{-1} is attributed to adsorbed water molecules. (e) XANES Co K-edge spectra of as-prepared ACFP series. For comparison, the spectra of CoO and $LiCoO_2$ are shown for reference samples of Co^{2+} and Co^{3+}, respectively. (f) XANES Fe K-edge spectra of as-prepared ACFP series. For comparison, the spectrum for Fe_2O_3 is shown for a reference sample of Fe^{3+}. The Insets in (e) and (f) show enlarged edge positions.

adsorption near edge structure (XANES) analysis was conducted. Fig. 2e and f present the Co and Fe K-edge XANES spectra of the ACFPs. The edge position in the XANES spectrum of ACP is well indexed to the Co(II)O reference, indicating that the initial oxidation of Co ions is +2 (Fig. 2e). On the other hand, the edge position in the XANES spectrum of AFP is consistent with that of the $Fe(III)_2O_3$ reference, indicative of an initial oxidation state of Fe ions of +3. Only slight changes of edge positions are observed for both Co and Fe spectra in the entire compositions of ACFP series, as shown in insets, indicating oxidation states of Co and Fe remain close to +2 and +3, respectively, in ACFPs regardless of the Co : Fe ratios. Consistently, X-ray photoelectron spectroscopy analyses also represent the Co^{2+} and Fe^{3+} oxidation states of surface elements for the entire compositions of ACFP series (Fig. S1†).

The electrochemical properties of the ACFP series were evaluated using cyclic voltammetry (CV) in a three-electrode beaker cell configuration in 1 M KOH electrolyte. The *iR*-corrected CVs indicate that the polarization curves (Fig. 3a) were substantially affected by the Co/Fe ratio, resulting in variance of the overpotential (η) with changing Fe content. For the ACP, the polarization curve exhibits a η of 364 mV with a standard deviation of 4 mV at a current density of 10 mA cm^{-2} (*i.e.* the current density (j) required to achieve 10% solar-to-fuel efficiency).[41] Notably, the η values for the same current density were significantly reduced with increasing Fe content until 40 at%. It was observed that ACFP82 was capable of delivering an η of 333 mV (standard deviation = 3 mV), and, more importantly, ACFP64 could present the smallest η of 329 mV (standard deviation = 5 mV) at $j = 10$ mA cm^{-2}. A further addition of Fe, however, led to a steady increase of η with the highest value recorded for AFP (see Fig. S3 and Table S2 in ESI† for the comparison of ACFP samples with benchmark catalysts). The Tafel slope of ACP was estimated to be approximately 63 mV dec^{-1} and was improved to ~41 mV dec^{-1} at 20 at% Fe (ACFP82) and to ~35 mV dec^{-1} in the range of 40–60 at% Fe (ACFP64 and 46) as shown in Fig. 3b. Further addition of Fe resulted in a slight increase in the Tafel slope up to 43 mV for AFP. The overall kinetic parameters measured for the ACFPs indicate that the catalytic activity gets substantially altered with the different ratios of Fe and Co in the phyllosilicates, achieving the highest activity at approximately 40 at% of Fe. The outstanding performance at the mixed Co and Fe compositions in the phyllosilicates over the ACP and AFP strongly suggests the synergistic effect of the two cations in the material. We emphasize that the enhanced OER properties of the ACFPs were not originated from other extrinsic factors such as the increase in the electrochemical surface area. As provided in Fig. S4 and S5 (ESI†), the relative surface area of electrodes simply decreases with increasing Fe content in the ACFPs, while higher catalytic activities were demonstrated for ACFP46 or 64 over ACP. It supports the idea that the high performance of ACFPs is likely due to the enhanced intrinsic catalytic activities in the Co–Fe mixed phyllosilicates, which will be elaborated later. Additionally, in Fig. 3c, we investigated the stability of ACFPs during the electrochemical water splitting. It presents that the voltage of ACFP64 remains almost invariant for continuous 24 hours electrochemical process under a constant j of 10 mA cm^{-2}.

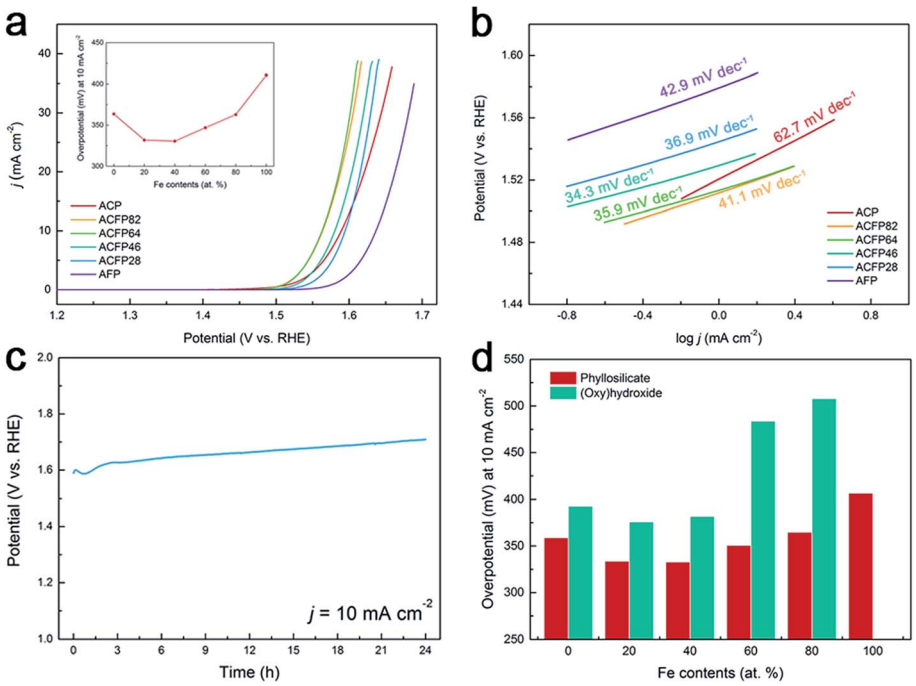

Fig. 3 OER catalysis characteristics of the prepared ACFP series. (a) *iR*-corrected polarization curves in 1 M KOH at a scan rate of 10 mV s^{-1}. Inset: trend of OER activities according to Fe contents in ACFP series. (b) Tafel plots of the ACFP series. (c) Long-term stability of ACFP64 at $j = 10$ mA cm^{-2} for 24 h. (d) Comparison of OER performance of phyllosilicate and (oxy)hydroxide catalysts based on the overpotential for a current density of 10 mA cm^{-2}. The overpotential value of pure Fe (oxy)hydroxide is not shown because it was extremely high, exceeding the range of the plot.

Notably, the trend of the OER characteristics of ACFPs as a function of the Co : Fe ratio is similar to the corresponding trends reported for Co–Fe (oxy)hydroxides, structural analogues of phyllosilicates.[35] Burke *et al.* synthesized $Co_{1-x}Fe_x(OOH)$ using electrodeposition and reported that the intrinsic OER activity of $Co_{1-x}Fe_x(OOH)$ was improved by ~100 fold upon changing the Fe content from $x = 0$ to $x = 0.6$–0.7 on a per-metal turnover frequency basis.[35] For a more precise and fair comparison of the OER properties of these with the phyllosilicates, we fabricated Co–Fe (oxy)hydroxides using the same co-precipitation method as that used for the phyllosilicates so that the extrinsic factors such as morphology, surface area and mass loading could be similarly controlled. Fig. 3d compares the OER performances of the phyllosilicates and (oxy)hydroxides at the same conditions for the entire Co : Fe composition range. It shows that the phyllosilicates exhibited much lower η than the (oxy)hydroxides for $j = 10$ mA cm^{-2} for the full range of metal compositions. This finding indicates the general beneficial role of the silicate layer for the OER catalysis in the Co–Fe binary layered system, consistent with our previous work.[23] The η of both the phyllosilicates and (oxy)hydroxides were smallest at Fe contents of 20–40 at%, implying a similar Co–Fe interaction for both structural motifs. For the Co–Fe (oxy)hydroxides, the Fe-rich (>60 at%) precipitates exhibited significantly high η values above 470 mV, whereas the η values of the phyllosilicates showed much less increase for the same Fe content range. This discrepancy can be attributed to the poor electrical conductivity of the FeOOH phase.[35,45] It is worthy of mentioning that the reported values of η for Co–Fe (oxy)hydroxides are slightly lower than those measured here, which is attributed to different surface area and mass loading for each study.[33,46] It suggests that further morphological engineering of phyllosilicates may lead to further increase in the catalytic activities.

To unveil the origin of the enhanced catalytic performance of the ACFPs compared with that of the ACPs at an atomistic level, comparative analysis of the OER thermodynamics was conducted using first-principles calculations on the surface of Fe-substituted ACP (see ESI,† for the details of the model construction). In a previous study, we showed that the presence of silicate groups on the layered motifs of cobalt (oxy)hydroxide produces diverse reaction sites with a distinct local environment and consequently assorted catalytic activities on the ACP surface.[23] The DFT calculations in the present work further reveal that the catalytic activities of such surficial reaction sites can be cumulatively modulated by structural perturbations induced by the Fe substitutions in the ACP motifs. Fig. 4a compares the theoretical η calculated for all the reaction sites of ACP and Fe-substituted ACP, including the bridge and terminal sites. On the ACP surface, the most catalytically active site was estimated to be bridge site 1, which provided a theoretical η of 0.34 V. The other sites on the ACP surface exhibited much higher theoretical η values above 0.54 V, suggesting that bridge site 1 is the primary active site in the catalysis of ACP. It is noteworthy that the substitution with Fe significantly modifies the activities of each reaction sites. The most prominent feature in the OER thermodynamics of Fe-substituted ACP is the promoted catalytic activity of bridge site 4. The incorporation of Fe markedly lowered the theoretical η of bridge site 4 from 0.81 to 0.32 V, indicating the generation of new active reaction sites. Moreover, the activity of bridge site 1 remained almost unchanged as its theoretical η only slightly increased from 0.34 to 0.39 V. The theoretical η values of the reaction sites other than bridge sites 1 and 4 were relatively high (above 0.50 V) in both bare and Fe-substituted ACP, preventing them from serving as major reaction sites in both cases. These findings demonstrate that the introduction of Fe into ACP provided an additional primary active site, *i.e.* bridge site 4, without compromising the activity of the existing active site, leading to the increased density of active sites on the surface.

We found that the catalytic activation of bridge site 4 on the Fe-substituted surface arises from the relatively flattened energy landscape in the OER process due to the modified adsorption energies of intermediates on this site. Fig. 4b compares the free energy landscapes for the OER occurring at the bridge site 4 of bare and Fe-substituted ACPs. The OER energies were evaluated assuming the acid–base mechanism and standard conditions ($T = 298.15$ K, $P = 1$ bar, and pH = 0) to be consistent with those in previous works (see ESI† for details of the computational method and OER mechanism).[47,48] The acid–base mechanism proceeds through four proton-coupled electron transfer (PCET) steps through which intermediates of OH*, O*, and OOH* are generated in turn. Each solid line in Fig. 4b indicates the energy level of the corresponding intermediate state relative to the initial state at 1.23 V *vs.* RHE, the thermodynamic equilibrium potential for water oxidation. For both bare and Fe-substituted ACPs, the third PCET step (*i.e.*, OOH* formation step) is predicted to be the potential-determining step at the bridge site 4. Interestingly, OOH* adsorption on bridge site 4 of Fe-substituted ACP requires much lower theoretical η than that of bare ACP, presenting that the catalytic activation of the bridge site 4 results from the more stable OOH* adsorption on the Fe-substituted ACP surface.

We suspect that the stabilization of OOH* formation is closely related to the structural modifications resulting from the existence of Fe on the surface. The inset of Fig. 4b illustrates that the substituted Fe ion is a next-nearest-neighbor metal of the bridge site 4 and regulates the distances between surficial atoms. Fig. 4c and d provide more detailed atomic configurations around bridge site 4 for the O (left panel) and OOH (right panel) intermediate states, corresponding to the third PCET step, in bare and Fe-substituted ACP, respectively. At the O* intermediate step, the bare ACP has two strong O–H bonds between the surficial atoms, as denoted by the red circle in Fig. 4c. As the positions of surficial atoms are reorganized with the adsorption of a water molecule on the active site (yellow dotted circle), one hydrogen bond disappears in the OOH* intermediate state. This loss of hydrogen bonding makes the OOH* state relatively unstable for the pure ACP surface.[49] On the other hand, the number and strength of hydrogen bonds are maintained almost similar for the Fe-substituted surface during the OOH* formation step (Fig. 4d). It is believed that the presence of Fe induces a larger oxygen–oxygen distance between the terminal oxygen coordinated to Fe from the surrounding terminal oxygens in the pristine material. Accordingly, the

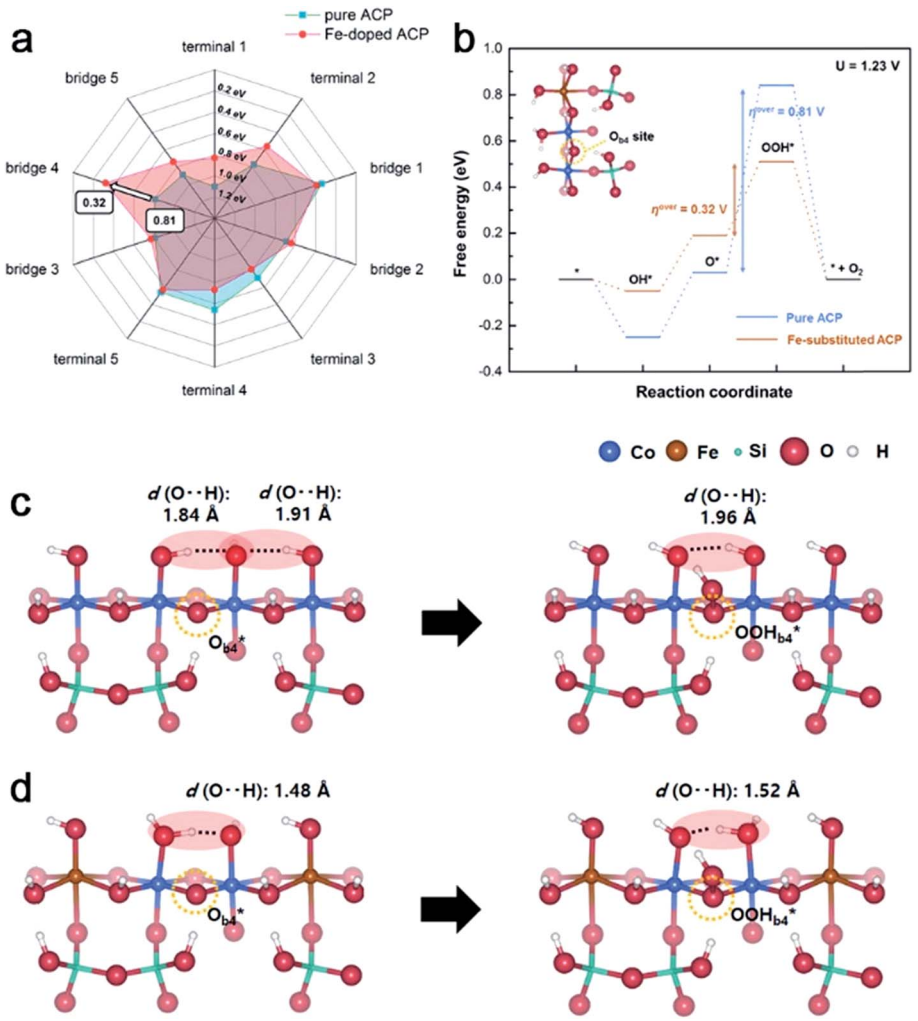

Fig. 4 DFT calculation results for the OER at pure and Fe-substituted ACP surfaces. (a) Comparison of theoretical η estimated for possible reaction sites of pure and Fe-substituted ACP surfaces. (b) Free energy landscape for the OER at 1.23 V *vs.* RHE. The blue and brown lines indicate the relative free energies of catalytic states appearing during the catalysis at bridge site 4 of pure and Fe-substituted ACP surfaces, respectively. (inset) Atomic configurations around bridge site 4 on the Fe-substituted ACP surface. Comparison of surface structures for the OOH* formation step at bridge site 4 on (c) pure ACP surface and (d) Fe-substituted ACP surface. Catalytic reaction sites and hydrogen bonding are denoted by yellow and red circles, respectively.

terminal oxygen of Fe cannot form strong O–H bonds with hydrogens bound to surrounding terminal oxygens irrespective of the O* or OOH* state, thereby allowing only one hydrogen bond between surficial atoms for both intermediate states. The substantial energy change due to the loss of hydrogen bonding during the OOH* formation step observed for the pure ACP is mitigated for the Fe-substituted case. These results suggest that the presence of Fe in the ACP motifs can result in local geometrical modulations of specific reaction sites, consequently leading to the flattened energy landscape, thus improved OER thermodynamics.

3. Conclusion

Our study demonstrates the possibility of using a multinary metal system for the development of earth-abundant layered phyllosilicate-based materials for water oxidation catalysis. The Co–Fe binary ACFPs introduced in this study were synthesized using a facile co-precipitation method at room temperature and delivered superior OER efficiencies (η of 329 mV for $j = 10$ mA cm^{-2}), far outperforming their unary phyllosilicate counterparts as well as Co–Fe (oxy)hydroxides. DFT calculations confirmed that the synergistic effect of Co and Fe ions in the phyllosilicate catalysts originated from the local structure modulation of reaction sites, which resulted in the provision of additional catalytic active sites. It proposes that layered phyllosilicate materials can be chemically tuned using various other combinations of metal elements to potentially lead to the development of novel high-performance phyllosilicate-based catalysts. Considering the structural similarity of layered phyllosilicates and layered metal (oxy)hydroxides, combinations of metals that have been reported to be successful for metal (oxy) hydroxide catalysts[41] are also likely to exhibit comparable or outperforming catalytic performance in the phyllosilicate

framework. Furthermore, we believe that the cumulative design strategy using ACFPs, which utilize both a redox-active metal and redox-inert polyanion elements, will provide valuable insight for the discovery of polyanion-based OER catalysts.

Conflicts of interest

There are no conflicts to declare.

Acknowledgements

This work was supported by the grant of National Research Foundation (NRF-2019M3E6A1064522), and the World Premier Materials grant funded by the Korea government Ministry of Trade, Industry and Energy.

References

1 Y. Tachibana, L. Vayssieres and J. R. Durrant, *Nat. Photonics*, 2012, **6**, 511.
2 M. Grätzel, *Nature*, 2001, **414**, 338.
3 T. Faunce, S. Styring, M. R. Wasielewski, G. W. Brudvig, A. W. Rutherford, J. Messinger, A. F. Lee, C. L. Hill, H. deGroot, M. Fontecave, D. R. MacFarlane, B. Hankamer, D. G. Nocera, D. M. Tiede, H. Dau, W. Hillier, L. Wang and R. Amal, *Energy Environ. Sci.*, 2013, **6**, 1074.
4 D. Gust, T. A. Moore and A. L. Moore, *Acc. Chem. Res.*, 2009, **42**, 1890.
5 K. Liang, S. Pakhira, Z. Yang, A. Nijamudheen, L. Ju, M. Wang, C. I. Aguirre-Velez, G. E. Sterbinsky, Y. Du, Z. Feng, J. L. Mendoza-Cortes and Y. Yang, *ACS Catal.*, 2019, **9**, 651.
6 T. A. Betley, Q. Wu, T. Van Voorhis and D. G. Nocera, *Inorg. Chem.*, 2008, **47**, 1849.
7 M. W. Kanan and D. G. Nocera, *Science*, 2008, **321**, 1072.
8 J. K. Hurst, *Science*, 2010, **328**, 315.
9 B. M. Hunter, H. B. Gray and A. M. Müller, *Chem. Rev.*, 2016, **116**, 14120.
10 R. Subbaraman, D. Tripkovic, K.-C. Chang, D. Strmcnik, A. P. Paulikas, P. Hirunsit, M. Chan, J. Greeley, V. Stamenkovic and N. M. Markovic, *Nat. Mater.*, 2012, **11**, 550.
11 B. Cui, H. Lin, J. B. Li, X. Li, J. Yang and J. Tao, *Adv. Funct. Mater.*, 2008, **18**, 1440.
12 H. Osgood, S. V. Devaguptapu, H. Xu, J. Cho and G. Wu, *Nano Today*, 2016, **11**, 601.
13 P. Du and R. Eisenberg, *Energy Environ. Sci.*, 2012, **5**, 6012.
14 W. Xu and H. Wang, *Chin. J. Catal.*, 2017, **38**, 991.
15 N.-T. Suen, S.-F. Hung, Q. Quan, N. Zhang, Y.-J. Xu and H. M. Chen, *Chem. Soc. Rev.*, 2017, **46**, 337.
16 J. Wang, W. Cui, Q. Liu, Z. Xing, M. Asiri Abdullah and X. Sun, *Adv. Mater.*, 2015, **28**, 215.
17 J. S. Kim, B. Kim, H. Kim and K. Kang, *Adv. Energy Mater.*, 2018, **8**, 1702774.
18 M. Dincă, Y. Surendranath and D. G. Nocera, *Proc. Natl. Acad. Sci. U. S. A.*, 2010, **107**, 10337.
19 A. M. Ullman, C. N. Brodsky, N. Li, S.-L. Zheng and D. G. Nocera, *J. Am. Chem. Soc.*, 2016, **138**, 4229.
20 F. Song and X. Hu, *Nat. Commun.*, 2014, **5**, 4477.
21 Y. Surendranath, D. A. Lutterman, Y. Liu and D. G. Nocera, *J. Am. Chem. Soc.*, 2012, **134**, 6326.
22 D. K. Bediako, B. Lassalle-Kaiser, Y. Surendranath, J. Yano, V. K. Yachandra and D. G. Nocera, *J. Am. Chem. Soc.*, 2012, **134**, 6801.
23 J. S. Kim, I. Park, E. S. Jeong, K. Jin, M. Seong Won, G. Yoon, H. Kim, B. Kim, T. Nam Ki and K. Kang, *Adv. Mater.*, 2017, **29**, 1606893.
24 J. Suntivich, K. J. May, H. A. Gasteiger, J. B. Goodenough and Y. Shao-Horn, *Science*, 2011, **334**, 1383.
25 M. García-Mota, A. Vojvodic, F. Abild-Pedersen and J. K. Nørskov, *J. Phys. Chem. C*, 2013, **117**, 460.
26 T. Bligaard and J. K. Nørskov, *Electrochim. Acta*, 2007, **52**, 5512.
27 Z. Xu and J. R. Kitchin, *J. Chem. Phys.*, 2015, **142**, 104703.
28 M. Bajdich, M. García-Mota, A. Vojvodic, J. K. Nørskov and A. T. Bell, *J. Am. Chem. Soc.*, 2013, **135**, 13521.
29 O. Diaz-Morales, I. Ledezma-Yanez, M. T. M. Koper and F. Calle-Vallejo, *ACS Catal.*, 2015, **5**, 5380.
30 P. Liao, J. A. Keith and E. A. Carter, *J. Am. Chem. Soc.*, 2012, **134**, 13296.
31 F. Dionigi and P. Strasser, *Adv. Energy Mater.*, 2016, **6**, 1600621.
32 L. Trotochaud, J. K. Ranney, K. N. Williams and S. W. Boettcher, *J. Am. Chem. Soc.*, 2012, **134**, 17253.
33 B. Zhang, X. Zheng, O. Voznyy, R. Comin, M. Bajdich, M. García-Melchor, L. Han, J. Xu, M. Liu, L. Zheng, F. P. García de Arquer, C. T. Dinh, F. Fan, M. Yuan, E. Yassitepe, N. Chen, T. Regier, P. Liu, Y. Li, P. De Luna, A. Janmohamed, H. L. Xin, H. Yang, A. Vojvodic and E. H. Sargent, *Science*, 2016, **352**, 333.
34 D. Friebel, M. W. Louie, M. Bajdich, K. E. Sanwald, Y. Cai, A. M. Wise, M.-J. Cheng, D. Sokaras, T.-C. Weng, R. Alonso-Mori, R. C. Davis, J. R. Bargar, J. K. Nørskov, A. Nilsson and A. T. Bell, *J. Am. Chem. Soc.*, 2015, **137**, 1305.
35 M. S. Burke, M. G. Kast, L. Trotochaud, A. M. Smith and S. W. Boettcher, *J. Am. Chem. Soc.*, 2015, **137**, 3638.
36 W. Niu, J. Shi, L. Ju, Z. Li, N. Orlovskaya, Y. Liu and Y. Yang, *ACS Catal.*, 2018, **8**, 12030.
37 R. D. L. Smith, M. S. Prévot, R. D. Fagan, S. Trudel and C. P. Berlinguette, *J. Am. Chem. Soc.*, 2013, **135**, 11580.
38 L. Gong, X. Y. E. Chng, Y. Du, S. Xi and B. S. Yeo, *ACS Catal.*, 2018, **8**, 807.
39 M. W. Louie and A. T. Bell, *J. Am. Chem. Soc.*, 2013, **135**, 12329.
40 H. Shin, H. Xiao and W. A. Goddard, *J. Am. Chem. Soc.*, 2018, **140**, 6745.
41 C. C. L. McCrory, S. Jung, I. M. Ferrer, S. M. Chatman, J. C. Peters and T. F. Jaramillo, *J. Am. Chem. Soc.*, 2015, **137**, 4347.
42 C. I. Sainz-Diaz, A. Hernández-Laguna and M. T. Dove, *Phys. Chem. Miner.*, 2001, **28**, 130.
43 A. R. Pawley and R. L. Jones, *Phys. Chem. Miner.*, 2011, **38**, 753.

44 R. Trujillano, J.-F. Lambert and C. Louis, *J. Phys. Chem. C*, 2008, **112**, 18551.
45 S. Zou, M. S. Burke, M. G. Kast, J. Fan, N. Danilovic and S. W. Boettcher, *Chem. Mater.*, 2015, **27**, 8011.
46 F. Yang, K. Sliozberg, I. Sinev, H. Antoni, A. Bähr, K. Ollegott, W. Xia, J. Masa, W. Grünert, B. R. Cuenya, W. Schuhmann and M. Muhler, *ChemSusChem*, 2017, **10**, 156.
47 J. Rossmeisl, Z. W. Qu, H. Zhu, G. J. Kroes and J. K. Nørskov, *J. Electroanal. Chem.*, 2007, **607**, 83.
48 I. C. Man, H.-Y. Su, F. Calle-Vallejo, H. A. Hansen, J. I. Martínez, N. G. Inoglu, J. Kitchin, T. F. Jaramillo, J. K. Nørskov and J. Rossmeisl, *ChemCatChem*, 2011, **3**, 1159.
49 P. Gilli, V. Bertolasi, V. Ferretti and G. Gilli, *J. Am. Chem. Soc.*, 1994, **116**, 909.